TASK QUARTERLY 7 No 4 (2003), 667–699

FE STUDIES OF QUASI-STATIC MASS FLOW IN BINS: THE POLAR ELASTO-PLASTIC APPROACH

JACEK TEJCHMAN

Civil Engineering Department, Gdansk University of Technology,
Narutowicza 11/12, 80-952 Gdansk, Poland
tejchmk@pg.gda.pl

(Received 11 May 2003)

Abstract: The paper deals with numerical modelling of confined flow of granular materials in vertical bins. Quasi-static mass flow of non-cohesive sand with a controlled outlet velocity along the entire silo bottom was numerically studied using a finite element method taking into account an elasto-plastic constitutive law laid down within a Cosserat continuum. The influence of the initial density and the mean grain diameter of the solid, wall roughness, wall stiffness and wall imperfection, the initial stress state and the pressure level on the stress and deformation states in plane-strain vertical bins was investigated. The numerical results were compared with similar model tests performed with a rectangular vertical bin containing sand. The calculated results were in satisfactory agreement with the experimental ones. The advantages and limitations of the polar elasto-plastic approach to model granular silo flow were outlined.

Keywords: elasto-plasticity, finite element method, flow, polar approach, silo

1. Introduction

The existing theoretical models of silo flow of granular materials can be divided into those treating the fill as a continuum or as separate particles. The former are more suitable for slow silo flow, *i.e.* flow with low deformation rates, where particles behave like a conglomerate and exhibit solidlike behaviour (grain contacts are preserved). During such flow, internal stresses are generated only by normal and friction forces among particles. The latter correspond to rapid silo flow, where the material behaves more like gas or dense fluid. Rapid flow is connected with high deformation rates and large inertial forces. During such flow, particles can lose contact and are subject to permanent short impulsive collisions and overriding. Internal stresses are created by normal and friction forces between grains and collisions. Both slow and rapid flow is dissipative. In slow flow, some energy is lost due to friction, as grains slide against each other. In rapid flow, the loss of energy is more pronounced because particle collisions are inherently inelastic. Both types of flow may occur simultaneously at various locations in a silo. Usually, the material at the outlet is in the rapid flow regime, whilst the material higher up is moving

slowly. Slow flow is mainly modelled in the continuum approach and rapid flow – using a discrete approach. Theoretical models describing the behaviour of granular materials within a continuum are mainly based on the finite element method. Discrete models use granular dynamics algorithms, kinetic theories or cellular automata approaches.

The aim of the theoretical research presented in this paper is to study the onset of quasi-static mass flow of granular materials in a plane strain vertical bin. Such flow often occurs in large silos when the material flows slowly and its outflow velocity is controlled. During such flow, many phenomena occur (sudden increase of wall stresses, shear zone formation, stress oscillation, non-uniform stress distribution) which have not been explained in detail yet. The study was performed with a continuum model based on the finite element method taking into account the polar elasto-plastic constitutive law. Inertia effects were neglected. The model has been formulated within continuum mechanics, but it has some properties characteristic for discrete models: it includes mean grain diameter, grain rotations and couple stresses. During FE calculations, the effect of the initial density, modulus of elasticity and mean grain diameter of the solid, initial stress state, wall roughness, wall stiffness and wall imperfection, as well as pressure level, on the material's behaviour was investigated. Additionally, the effect of large deformations and curvatures, as well as micro-polar constants was analysed. The FE results were compared with the corresponding model tests carried out in a rectangular model silo with parallel walls and a slowly movable bottom.

The existing FEM solutions of silo flow [1–13] are more realistic than analytical formulae to calculate loads in silos, since they are able to calculate deformations and stresses at each point of the silo fill. However, most of them have been obtained within a classical continuum and, thus, the obtained results are dependent on the magnitude of the element mesh [5–8, 10–12]. Moreover, some of them have not considered the material's softening [5–8, 10, 11] caused by the formation of shear zones, a factor of major importance for dense granular bodies [1, 4]. They have also been unable to consistently describe the interface behaviour along the silo wall [5–8, 10–12]. The influence of wall roughness on the behaviour of flow was not systematically investigated either [5–12]. A great advantage of finite element simulations as compared to discrete methods is their ability to consider large systems, while the material constants in continuum constitutive models can be calibrated with standard laboratory tests. However, granular dynamics models [14–21] still require too much computer time and they are, thus, not applicable to large silos. Moreover, the determination of micro-structural material parameters and wall boundary conditions is difficult in these models. There is simply a lack of experimental data on micro-structural parameters that could help better calibrate granular dynamics models. The identification of material constants and the assumption of realistic wall boundary conditions in analytical kinetic theories [22–26] is also difficult. At the same time, cellular automata approaches are purely kinematic models [27, 28], and as such, they are not suitable to realistically describe confined flow in silos and to calculate stresses in the fill.

2. Model tests

Experiments were carried out with dry sand (mean grain diameter $d_{50} = 0.50\,\text{mm}$) in a rectangular container with a slowly movable bottom [1, 29, 30]. The silo height was $h = 0.50\,\text{m}$, its length was $l = 0.60\,\text{m}$ and its width – $b = 0.10$–$0.30\,\text{m}$. Three resultant forces were measured during filling and emptying: the vertical wall friction force, the vertical bottom force and the horizontal force on the wall. Additionally, the bottom is displacement and the displacement of the upper fill surface were recorded. Quasi-static mass discharge was simulated by slowly lowering a bottom plate with a constant velocity of 5 mm/h. The model tests were performed with three degrees of wall roughness. The roughness r_w is depicted as a relative height between the highest and the lowest point along the surface at a length of $(3$–$4)\times d_{50}$ [1, 31, 32]. The silo walls were smooth ($r_w \approx 0$), rough ($0 < r_w < d_{50}$) or very rough ($r_w \geq d_{50}$). The fill was loose (initial density $\gamma_d = 14.50\,\text{kN/m}^3$, initial void ratio $e_0 = 0.83$), medium dense ($\gamma_d = 15.75$–$16.30\,\text{kN/m}^3$, $e_0 = 0.63$–0.69) or dense ($\gamma_d = 16.75\,\text{kN/m3}$, $e_0 = 0.60$).

The sand's flow was of the plug type, except for a narrow shear zone adjacent to the wall [1, 29, 30]. For very rough walls and dense sand, secondary shear zones were created inside the fill. They first appeared in the lower region of the silo above the outlet and then propagated upwards causing a non-symmetry of flow. The thickness of the wall shear zone was found to be approximately 5 mm ($10 \times d_{50}$) for smooth walls, 20 mm ($40 \times d_{50}$) for very rough walls and loose sand, and 15 mm ($30 \times d_{50}$) for very rough walls and dense sand. During filling, the maximum wall shear force was reached for very rough walls and dense sand; it increased with increasing wall roughness and initial sand density. The maximum horizontal wall force during filling was observed in loose sand with smooth walls; it decreased with increasing fill density and wall roughness. The emptying tests [1] showed that the greater the roughness of silo walls and the initial density of bulk solids, the smaller the minimum bottom force after bottom displacement, and the larger the wall friction force, and angle and material softening in the wall shear zone. The changes of forces during emptying were insignificant for loose sand. The maximum horizontal force on the wall occurred for rough walls and dense sand, and the minimum horizontal force appeared for smooth walls and dense sand. In the case of very rough walls, the maximum horizontal wall force occured for medium dense sand. Thus, no unique relationship between the horizontal wall force and wall roughness or fill density was found. Only for loose sand, the horizontal wall force behaved qualitatively almost according to the Janssen equation [33] (an increase of the force with a decrease of wall roughness). The shape of the horizontal wall force depended upon the silo's width (an increase of the normalised normal force with decreasing silo width was observed). The measured forces always reached a residual state. During flow, dense and medium dense sand first experienced dilatancy, followed by an insignificant contractancy in the residual state; loose sand only densified during flow. To investigate the effect of the mean grain diameter on the thickness of the wall shear zone, experiments were carried out with the same sand, but using only grains larger than 1.0 mm. In this case, the thickness of the shear zone was about 2–2.5 cm in the silo with very rough walls.

The maximum wall forces T and N were approximated by a slice method using the Janssen equation [33] for plane strain to calculate mean pressure coefficients

$\bar{K} = \sigma_{11}^w / \sigma_{22}^m$ (σ_{11}^w – horizontal wall normal stress, σ_{22}^m – mean vertical normal stress). We have obtained the following maximum values of $\bar{K}$: 0.24–0.29 (dense sand) and 0.36–0.39 (loose sand) for filling ($b = 0.20$m), and 0.30–0.73 (dense sand) and 0.37–0.50 (loose sand) for emptying ($b = 0.20$m). Thus, the $\bar{K}$ coefficients were greater with increasing initial sand density during emptying and decreasing initial sand density during filling. In any case, they increased with increasing wall roughness.

3. Plane polar continuum

A polar (Cosserat) continuum differs from a classical (non-polar) continuum in that an additional rotation, ω^c, appears in its kinematics [34, 35]. Thus, each material point of the plane polar continuum has three degrees of freedom: two translational degrees of freedom, u_1 and u_2, and a rotational degree of freedom, ω^c (Figure 1a). The state of deformation within a polar continuum is described by the following six deformation quantities (which are considered here to be infinitesimal):

$$\varepsilon_{11} = u_{1,1}, \qquad \varepsilon_{22} = u_{2,2}, \tag{1}$$

$$\varepsilon_{12} = u_{1,2} + \omega^c, \qquad \varepsilon_{21} = u_{2,1} - \omega^c, \tag{2}$$

$$\kappa_1 = \omega^c_{,1}, \qquad \kappa_2 = \omega^c_{,2}, \tag{3}$$

where

$$()_{,i} = \partial() / \partial x_i. \tag{4}$$

ε_{ij} are components of the deformation tensor, and κ_i are components of the curvature vector. The normal deformations ε_{ii} are defined similarly as in a non-polar continuum. The shear deformations ε_{12} and ε_{21} can be viewed as relative deformations relating the macro-displacement gradient and micro-rotation; in contrast to a non-polar continuum, $\varepsilon_{12} \neq \varepsilon_{21}$. The curvatures κ_1 and κ_2 describe the macro-deformation gradients of micro-rotation. The quantities ε_{ij} and κ_i are invariant with respect to rigid body motions [36, 37]. Six deformation quantities are conjugate with respect to energy to six stress quantities referred to the actual configuration. The four components of ε_{ij} are associated with the four components of the stress tensor σ_{ij}, which is generally non-symmetric ($\sigma_{12} \neq \sigma_{21}$). The curvatures κ_i are associated with the couple stresses m_i. Figure 1b shows the stresses and couple stresses at an

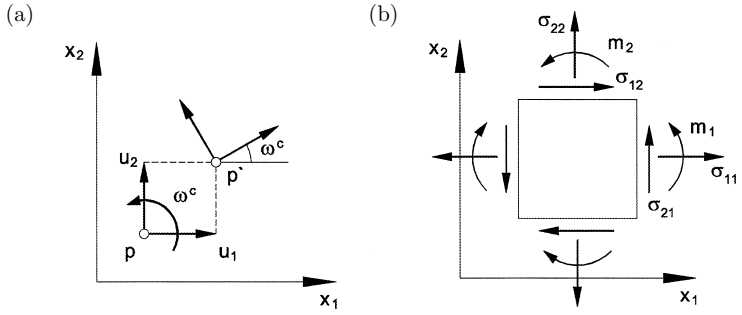

Figure 1. Plane Cosserat continuum (without volume loads):
(a) degrees of freedom (u_1, u_2 – horizontal and vertical displacement, ω^c – Cosserat rotation),
(b) stresses, σ_{ij}, and couple stresses, m_i, at an element

infinitesimal element (dx_1, dx_2) of a plane Cosserat continuum. The force equilibrium and the moment equilibrium give the following equations of motion:

$$\sigma_{11,1}+\sigma_{12,2}-f_1^B=0, \tag{5}$$

$$\sigma_{21,1}+\sigma_{22,2}-f_2^B=0, \tag{6}$$

$$m_{1,1}+m_{2,2}+\sigma_{21}-\sigma_{12}-m^B=0, \tag{7}$$

where f_i^B are the volume body forces and m^B denotes the volume body moment. The equilibrium conditions (Equations (5)–(7)) are equivalent to the virtual work principle:

$$\int_B (\sigma_{ij}\delta\varepsilon_{ij}+m_i\delta\kappa_i)\,dV=\int_B \left[f_i^B\delta u_i+m^B\delta\omega^c\right]dV+\int_{\partial_1 B} t_i\delta u_i dA+\int_{\partial_2 B} m\delta\omega^c dA, \tag{8}$$

where

$$\sigma_{ij}n_j=t_i \quad \text{on} \quad \partial_1 B, \quad m_i n_i=m \quad \text{on} \quad \partial_2 B. \tag{9}$$

t_i and m are prescribed boundary tractions and moment, respectively; $\delta\varepsilon_{ij}$ and $\delta\kappa_i$ denote virtual deformations and curvatures; δu_i is virtual displacement; $\delta\omega^c$ is the virtual Cosserat rotation and V is body volume. Virtual displacements and the virtual Cosserat rotations disappear on those parts of the boundary where the kinematic boundary conditions are prescribed. The work principle states that the fields σ_{ij}, m_i satisfying for arbitrary kinematically admissible virtual δu_i, $\delta\omega^c$ also satisfy the equilibrium conditions (Equations (5)–(7)) and the boundary conditions (Equation (9)). The virtual work principle is used to formulate an FEM of motion [1, 4, 37]. As a consequence of the presence of rotations and couple stresses, the constitutive law for granular materials within a polar continuum is endowed with a characteristic length corresponding to the mean grain diameter. Thus, the numerical results are not sensitive to spatial discretisation [1, 4, 37, 38], and boundary value problems remain mathematically well-posed [38–40] when using softening constitutive laws. Due to the presence of a characteristic length, a polar approach can model the thickness of shear zones and related grain size effects in granulates [4]. Otherwise, numerical calculations with constitutive laws without a characteristic length produce unreliable results. Shear zones become narrower upon mesh refinement and computed load-displacements curves change considerably [1]. A polar approach is more suitable to model shear zones in granulates as compared to other models able to capture localisation of deformations in a proper manner (*e.g.* non-local, strain gradient and viscous models [38]) on better physical grounds, since it takes into account rotations and couple stresses, which are observed during shearing [41–43] but remain negligible during homogeneous deformation. A polar model is stiffer and stronger than a non-polar one because the work of a Cosserat continuum (Equation (8)) is augmented by couple stresses, curvatures and rotations depending upon the mean grain size. Thus, the additional degree of freedom of a polar continuum releases additional resistance against itself (which corresponds, for instance, to the overstiffening of a hinge joint of a frame by prescribing an additional moment). The FE calculations have shown that the thickness of shear zones depends insignificantly upon mesh refinement if the size of finite elements in the shear zone is not greater than five times the mean

grain diameter (when using triangular finite elements with linear shape functions for displacements and a Cosserat rotation, see [1, 4, 43]).

4. Polar elasto-plastic constitutive relation

Bogdanova-Bontscheva and Lippmann [44] showed for the first time that Cosserat type rotations appear during shearing of granular materials. Further studies by Becker and Lippmann [45] and Kanatani [46] demonstrated that the Cosserat effects are of major importance only along the boundaries. A Cosserat elasto-plastic constitutive model for granular materials with isotropic hardening and softening was proposed by Mühlhaus [37] and further developed by Mühlhaus und Vardoulakis [47] and Mühlhaus [48, 49]. It differs from the conventional constitutive law of Drucker-Prager in the presence of Cosserat rotations and couple stresses using the mean grain diameter as a characteristic length. It can be summarised as follows:

$$\dot{\varepsilon}_{ij} = \dot{\varepsilon}^e_{ij} + \dot{\varepsilon}^p_{ij}, \qquad \dot{\kappa}_i = \dot{\kappa}^e_i + \dot{\kappa}^p_i, \tag{10}$$

$$\dot{\varepsilon}^e_{ij} = \frac{1}{E}[(1+\nu)\dot{\sigma}_{ij} - \nu\dot{\sigma}_{kk}], \qquad i = k, \tag{11}$$

$$\dot{\varepsilon}^e_{ij} = \frac{1}{2G}\frac{\partial\dot{\tau}^2}{\partial\sigma_{ij}}, \qquad \dot{\kappa}^e_i = \frac{1}{2G}\frac{\partial\dot{\tau}^2}{\partial m_i}, \qquad i \neq j, \tag{12}$$

$$\dot{\varepsilon}^p_{ij} = \lambda\frac{\partial g}{\partial\sigma_{ij}}, \qquad \dot{\kappa}^p_i = \lambda\frac{\partial g}{\partial m_i}, \tag{13}$$

$$\tau = (a_1 s_{ij}s_{ij} + a_2 s_{ij}s_{ji} + \frac{a_3}{d_{50}^2} m_i m_i)^{1/2}, \tag{14}$$

$$f = \tau + \mu(e_0, \gamma^p)p - c, \tag{15}$$

$$g = \tau + \alpha(e_0, \gamma^p)p, \tag{16}$$

$$\mu = \sin\phi, \tag{17}$$

$$\alpha = \sin\beta, \tag{18}$$

wherein τ is the second invariant of the deviatoric stress tensor, s_{ij} – the non-symmetric deviatoric stress tensor ($s_{ij} = \sigma_{ij} - p\delta_{ij}$), p – mean stress ($p = 1/2\sigma_{ii}$), σ_{ij} – the stress tensor, m_i – the couple stress vector, a_1, a_2 and a_3 – micro-polar coefficients, d_{50} – mean grain diameter, f – the yield function, g – the potential function, μ – the mobilised friction factor, α – the mobilised dilatancy factor, ϕ – the internal friction angle, β – the dilatancy angle, e_0 – the initial void ratio, c – cohesion, γ^p – plastic shear deformation, ε_{ij} – the deformation tensor, $\dot{\varepsilon}_{ij}$ – the rate of deformation tensor, κ_i – the curvature vector, $\dot{\kappa}_i$ – the rate of curvature vector, λ

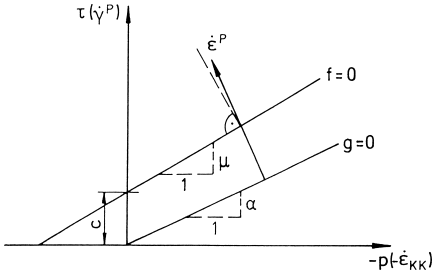

Figure 2. Yield curve $f = 0$ and flow potential curve $g = 0$ in the τ, p plane

– the proportionality factor, E – the elastic modulus, G – the shear modulus, ν – the Poisson ratio, δ_{ij} – the Kronecker delta. The superimposed indexes e and p designate the elastic and the plastic strain or curvature, respectively. The meaning of f, g, τ, γ^p and λ is analogous to that in non-polar plasticity [50]. The equations $f=0$ and $g=0$ describe a yield curve and a flow potential curve, respectively (Figure 2). The factor λ is calculated from the consistency condition $df=0$. The expression for τ in Equation (14) was determined with the aid of the plastic shear strain rate $\dot{\gamma}^p$ which had been derived on the macroscopic level by taking into account slip and rotation in a random assembly of circular rods with a diameter d_{50} [49]. If the moment stress vector m_i disappears, τ in Equation (14) is reduced to its counterpart in a non-polar continuum:

$$\tau = (s_{ij}s_{ij})^{0.5}. \tag{19}$$

The micro-polar constants a_1, a_2 and a_3 (Equation (14)) control the influence of the Cosserat quantities on the material's behaviour. The smaller the difference between a_1 and a_2, the greater the non-symmetry of the stress tensor and the effect of the Cosserat quantities on the material's behaviour [4, 51]. All combinations of the constants a_1 and a_2 are theoretically possible, provided that $a_1+a_2=0.5$ [49]. The influence of a_3 on the results is rather insignificant [4]. Since the coefficients a_1, a_2 and a_3 are micro-polar constants, they can be generally found with comparative FE calculations [4]. The factors μ in Equation (15) and α in Equation (16), which are related to the angle of internal friction, ϕ (Equation (17)), and the angle of dilatancy, β (Equation (18)), of granular materials, can be identified for plane-strain problems with tests in a plane-strain apparatus [52], Figure 3.

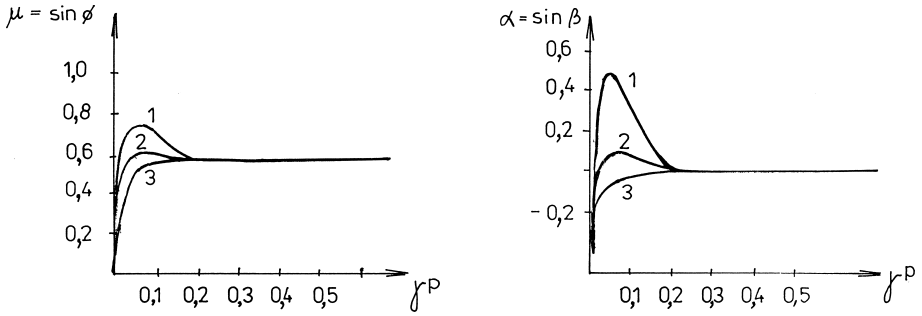

Figure 3. Mobilised friction factor, μ, and mobilised dilatancy factor, α, for granular materials (ϕ – angle of internal friction, β – dilatancy angle, γ^p – plastic shear deformation); 1 – dense sand, 2 – medium dense sand, 3 – loose sand

The outlined constitutive law includes the following constants or functions to be determined for non-cohesive granular materials: the modulus of elasticity E; Poisson's ratio, ν; the internal friction angle, ϕ, versus plastic shear deformation, γ^p; the dilatancy angle, β, versus plastic shear deformation, γ^p; mean grain diameter, d_{50}; and the micro-polar coefficients a_1, a_2 and a_3. The coefficient E can be assessed for quasi-static silo flow problems with a formula for oedometric unloading [4]:

$$E = \frac{1+e_0}{C_s}p, \tag{20}$$

wherein e_0 is the initial void ratio, C_s denotes the swelling index, and p is the mean stress. Poisson's ratio, ν, was chosen as 0.30 [52]. The mean grain diameter can be determined in a standard laboratory test.

The capability of an elasto-plastic Cosserat model for solving various boundary-value problems involving localisation was demonstrated by Tejchman [1, 4, 53], Mühlhaus [36, 37, 48, 49], de Borst [54], Papanastasiou and Vardoulakis [55], Sluys [38], Tejchman and Wu [51, 56, 57], Tejchman and Gudehus [2], Unterreiner *et al.* [58], Steinmann [59], Murakami and Yoshida [60] and Groen [61].

5. Finite element implementation

For the plane-strain calculations of the onset of granular flow in the model silo ($h = 0.50$m, $b = 0.20$m) of Section 2, an FE mesh with quadrilateral finite elements composed of four diagonally crossed triangles was applied to avoid volumetric locking and spurious element behaviour [61]. A total of 3 000 triangular elements were used (Figure 4) with linear shape functions for the displacements and the Cosserat rotation. Symmetry with respect to the centre line was taken into account. In order to realistically describe the interface behaviour along the wall, the FE mesh was significantly refined at the wall. The width of quadrilateral elements close to the wall was equal to 0.5mm, 1.5mm and 3mm, respectively. The height of all quadrilateral elements was 10mm.

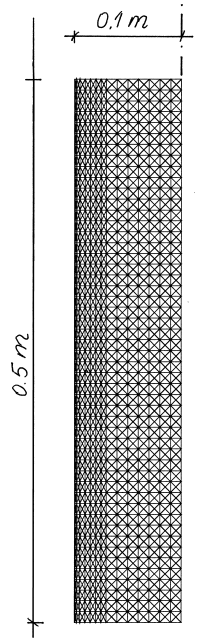

Figure 4. The mesh assumed for FE calculations

Calculations were performed both with a changing and a constant elastic modulus E calculated from Equation (20). In the former case, we assumed $E \cong 500p$ (with $e_0 = 0.60$–83 and $C_s = 0.003$–0.004 [62]), in the latter case – $E = 500 \cdot 4.0 = 2\,000$kPa (with $p \cong 4.0$kPa on the basis of initial calculations).

As an initial stress state before lowering the bottom, the stresses σ_{ij} after filling according to Janssen's [33] slice method for plane strain were assumed (with couple stresses m_i being zero):

$$\sigma_{22} = \frac{\gamma_d b}{2K\tan\varphi_w}\left[1-\exp\left(\frac{-2K\tan\varphi_w x_2}{b}\right)\right], \tag{21}$$

$$\sigma_{11} = K\sigma_{22}, \tag{22}$$

$$\sigma_{12} = \sigma_{21} = \sigma_{11}\tan\varphi_w(1-2x_1/b), \tag{23}$$

wherein K is the mean pressure coefficient, φ_w denotes the wall friction angle, x_2 is the vertical coordinate measured from the top of the fill, x_1 is the horizontal coordinate measured from the wall, and b denotes the silo's width. On the basis of model tests, we chose: $K=0.29$ and $\varphi_w=43^\circ$ (very rough walls, dense sand), $K=0.39$ and $\varphi_w=39^\circ$ (very rough walls and medium dense sand), $K=0.39$ and $\varphi_w=32^\circ$ (very rough walls and loose sand), $K=0.27$ and $\varphi_w=36^\circ$ (rough walls and dense sand), $K=0.24$ and $\varphi_w=15^\circ$ (smooth walls and dense sand). Both model experiments [1] and numerical calculations [63] show that stresses in silos due to filling can be approximated with a slice method, provided that K and φ_w have been estimated empirically. The FE calculations began with $\gamma_p=0.03$, corresponding to $\phi=35^\circ$ and $\beta=0^\circ$ (dense and medium dense sand) and $\phi=34.0^\circ$ and $\beta=-8^\circ$ (loose sand).

The Cosserat boundary conditions in a polar continuum allow for the variety in wall roughness. The numerical calculations were performed with smooth walls ($r_w \ll d_{50}$), rough walls ($0<r_w<d_{50}$), and very rough walls ($r_w \geq d_{50}$). For modelling very rough silo walls, full shearing of the material along a non-movable wall was assumed [4, 63]:

$$u_1=0, \qquad u_2=0, \qquad \omega^c=0. \tag{24}$$

In the case of smooth silo walls, both shearing and slip of the material along a rigid wall was taken into account. The calculations were carried out with the following assumptions [4, 63]:

$$u_1=0, \qquad \omega^c/u_2=-r_w/d_{50}^2. \tag{25}$$

Assuming a relationship between the couple stress m_1 and the vertical shear stress σ_{21}, the third condition is obtained automatically. In the residual state, it is approximately equal to $m_1/\sigma_{21}=d_{50}^2/r_w$ [4].

The r_w/d_{50} ratio was chosen to be 0.05 for smooth walls and 0.25 and 0.50 for rough walls. The boundary conditions assumed in Equation (25) turned out to be realistic and consistent, *i.e.* for $r_w/d_{50}\approx 0$, no stress changes in the material were observed, and for $r_w/d_{50}=0.5$–1.0 (depending on the micro-polar constants), the numerical results approached the results for very rough walls with the boundary conditions expressed by Equation (24) [63]. As a result of the assumed polar boundary conditions on the wall, the wall friction angle was derived and no special interface elements were needed [4]. The remaining boundary conditions in the silo fill were along the top traction and moment free, and in the symmetry axis: $u_1=0$, $\omega^c=0$, $\sigma_{21}=0$.

Quasi-static mass flow was initiated through constant vertical displacement increments prescribed to all nodes along the bottom. The displacement increment

was 0.025mm. In the case of very rough walls, the bottom node on the wall was also kept fixed.

The calculations were carried out with large deformations and curvatures. In this case, an updated Lagrangian formulation [64] was applied using the Jaumann stress rate and couple stress rate. At the same time, changes in the configuration and volume of elements were taken into account.

To satisfy the consistency condition $f=0$, the trial stress method was applied (linearised expansion of the yield condition about the trial stress point) using an elastic predictor and a plastic corrector with radial return mapping algorithm [65]. The integration was performed at 3 sample points placed in the middle of each triangular element side.

The volume body moment m^B (Equation (7)) was neglected. Initial calculations showed that $m^B = \pm\gamma_d(d_{50}/2)$ had a rather insignificant influence on the results [4]. The density of the silo fill was kept constant during the FE analyses.

To solve the non-linear equation of motion governing the response of a system of finite elements, a modified Newton-Raphson scheme was used. The calculations were performed using a symmetric, elastic global stiffness matrix. To accelerate the convergency, the increments of the initial displacements and rotations in each new calculation step were assumed to be equal to the total increments calculated in the previous step [4]. For the calculations with a changing elastic modulus, the global elastic stiffness matrix was updated every few steps. The iteration steps were performed using translation and rotation convergence criteria (found in preliminary FE calculations).

Tensile normal stresses were not allowed in the silo fill. If they were obtained in some elements, the normal stresses, shear stresses and couple stresses in these elements were replaced by zero values. For such elements, the element elastic stiffness matrix was either significantly reduced or assumed to be equal to the initial elastic one.

6. Numerical results

Figures 5–25 present numerical results of the finite element simulation of quasi-static mass flow in a plane-strain silo with parallel walls. During the FE calculations, the effect of the following parameters on the material behaviour was carefully investigated:

- initial sand density,
- wall roughness,
- the modulus of elasticity,
- the initial stress state in the silo,
- the mean grain diameter of sand,
- the polar coefficients,
- wall stiffness,
- wall imperfections and
- the pressure level.

Additionally, the effect of small deformations and curvatures was analysed. The calculations investigating the effect of the initial fill density and wall roughness

(carried out with a changing elastic modulus E) were compared with the model tests of Section 2. Other parameter studies were performed with a constant modulus of elasticity and mainly with very rough walls, where the largest changes of forces occur during confined granular flow. During the FE calculations, the evolution of the resultant wall forces T and N was closely followed, as well as that of, the resultant bottom force P, the horizontal wall stresses during silo flow, and the thickness of the wall shear zone. The resultant forces T, N and P were calculated as the total sum of all vertical or horizontal nodal forces along the wall or all vertical nodal forces along the bottom, respectively. The wall stresses were obtained from nodal forces along the wall. To compare the calculated forces (plane strain, $l = 1\,\mathrm{m}$) with the experimental ones (obtained in a rectangular bin with a length of $l = 0.60\,\mathrm{m}$), the calculated values of P, T and N were reduced by multiplying them by the factor 0.6. However, the calculated stresses were left unchanged.

6.1. Influence of the initial sand density

Figures 5–11 show the results for dense sand ($\gamma_d = 16.75\,\mathrm{kN/m^3}$, $E = 500p\,\mathrm{kPa}$, $\nu = 0.3$, $\phi_{\max} = 47^\circ$, $\phi_{\mathrm{cr}} = 35^\circ$, $\beta_{\max} = 28.3^\circ$, $\beta_{\mathrm{cr}} = 0^\circ$, $\gamma_p^p = 0.05$, $\gamma_{\mathrm{cr}}^p = 0.20$, $d_{50} = 0.50\,\mathrm{mm}$, $a_1 = 0.30$, $a_2 = 0.20$, $a_3 = 1.0$) in a silo with very rough parallel walls ($h = 0.50\,\mathrm{m}$, $b = 0.20\,\mathrm{m}$). $\phi_{\max}$ and ϕ_{cr} are the internal friction angle at peak and in the residual state, respectively (Figure 3). $\beta_{\max}$ and β_{cr} denote the dilatancy angle at peak and in the residual state, respectively (Figure 3). The plastic shear deformation at peak and the plastic shear deformation at $\beta = 0^\circ$ are described as γ_p^p and γ_{cr}^p, respectively (Figure 3). The calculated resultant P, T and N forces and the resultant wall friction angle $\varphi_w = \mathrm{arctg}(T/N)$ versus the vertical bottom displacement u_2^b are presented in Figure 5. The calculated stresses and couple stresses at various points of the solid are depicted in Figures 6 and 7. The horizontal wall stresses σ_{11} were obtained from the division of horizontal nodal forces along the wall by the node distance or calculated as the mean values in the triangular elements located directly at the wall. In both cases, very similar values of σ_{11} were obtained. The evolution of the wall pressure coefficients $K = \sigma_{11}/\sigma_{22}$ is shown in Figure 8. The results of the vertical displacement u_2, the Cosserat rotation ω^c and stresses σ_{ij} (mean values from quadrilateral elements) along the silo width at half the silo's height are described in Figure 9. The calculated displacements and Cosserat rotations are depicted in Figure 10. The magnitude of the Cosserat rotation was marked by circles with a maximum diameter corresponding to the maximum value in the given step. The distribution of stresses σ_{11}, σ_{22} and σ_{21} in all triangular elements of the mesh are presented in Figure 11. The darker the region, the lower the absolute stress value.

The calculated results of forces P, T and N (Figure 10) are in satisfactory agreement with the experimental ones [1]. They reach their asymptotes in a way similar to that of the measured curves, but some discrepancies occur: the calculated maximum and residual N forces are too great compared to the experimental results, while the minimum bottom force P is too small. However, the residual bottom force P is in good accordance. The calculated maximum resultant wall friction angle $\varphi_w = 48^\circ$ and the residual wall friction angle $\varphi_w = 32^\circ$ are close to the experimental values [1]. In general, the solid's behaviour is similar to that during simple shearing [4].

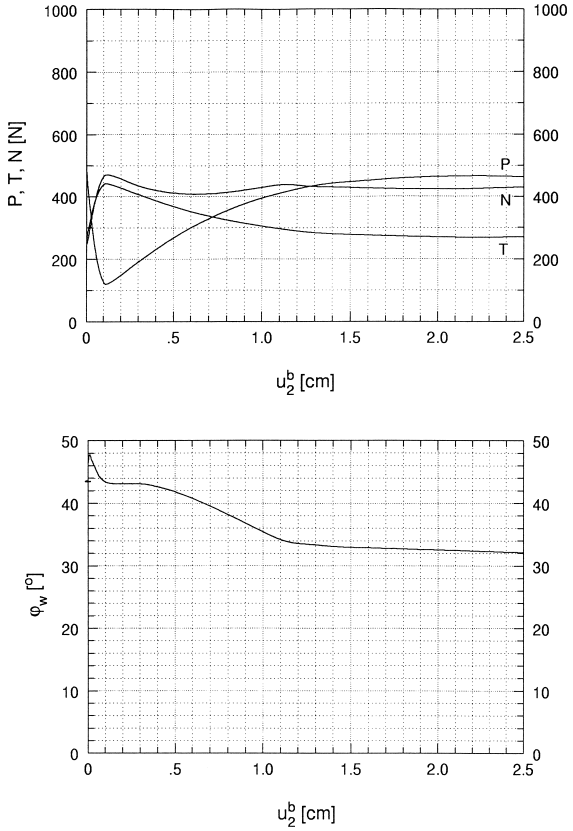

Figure 5. FE results for dense sand and very rough walls: evolution of resultant forces P, T, N and wall friction angle, $\varphi_w = \mathrm{arctg}(T/N)$, versus bottom displacement, u_2^b (T – vertical wall friction force, N – horizontal wall force, P – vertical bottom force)

The calculated horizontal wall stresses show clear peaks at the beginning of shearing and subsequently decrease, reaching a residual state (Figure 6). They indicate a tendency to oscillate. The maximum horizontal wall stresses, $\sigma_{11}^{\max} = 3.4$–$3.6\,\mathrm{kPa}$, are significantly higher than those calculated for very rough walls by the German Silo Code (plane strain), $\sigma_{11} = 2.45\,\mathrm{kPa}$, with $\gamma_d = 16.75\,\mathrm{kN/m^3}$, $K = 0.70$ and $\mu = \tan\varphi_w = 0.6$. Since the peaks of horizontal stresses along the wall are displaced in time, the maximum horizontal wall force is not very high. The distribution of stresses along the wall significantly differs from that obtained with the slice method of Janssen [33]. The behaviour of vertical wall shear stresses and wall couple stresses is similar to that of σ_{11} (Figure 7). The shape of the curves $\sigma_{22} = f(u_2^b)$ is similar to that of the calculated bottom force P.

Cosserat rotations, couple stresses and the non-symmetry of the stress tensor are noticeable only in the wall shear zone (Figures 9 and 10). The thickness of the wall shear zone, based on the vertical displacement and the Cosserat rotation, is 17.0 mm (Figure 10), and compares well with the experimental value [1]. It can therefore be assumed that only Cosserat rotations greater than 0.1 (at $u_2^b = 25\,\mathrm{mm}$) are significant in the shear zone.

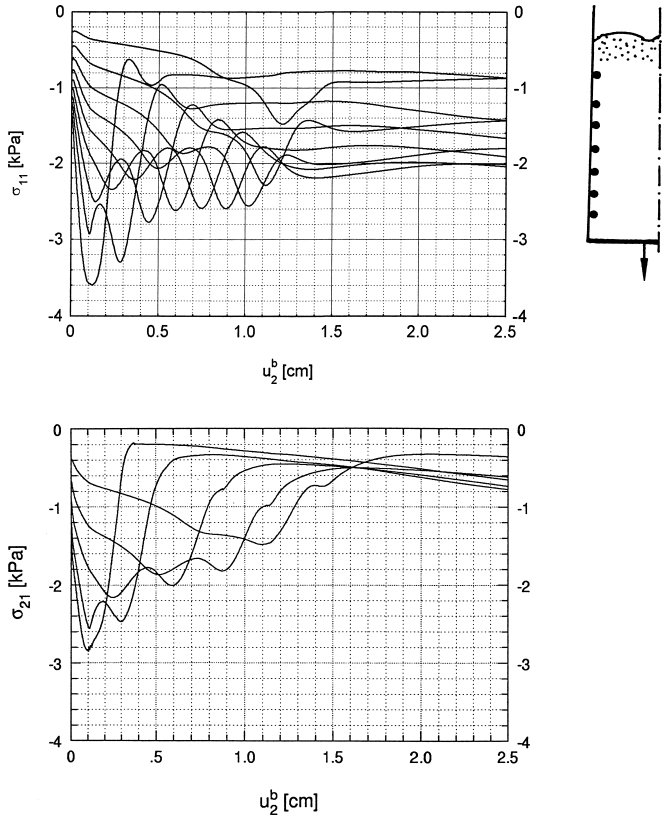

Figure 6. Calculated horizontal normal stresses, σ_{11}, and vertical shear stresses, σ_{21}, versus bottom displacement, u_2^b, at various points along the wall (dense sand, very rough walls)

The stresses σ_{ij} are not uniformly distributed in the entire silo (Figures 9 and 11). The residual pressure coefficients are always 1 in the wall shear zone (Figures 8 and 9). The mean pressure coefficients are about 0.8–0.9. The ratio between the wall couple stress m_1^w and the vertical shear stress σ_{21}^w along the wall is approximately 0.50 in the residual state.

The mean volume changes $(u-w)/h = 0.018$ in the residual state are in accordance with the experiment [1].

The results for medium dense sand ($\gamma_d = 15.20\text{kN/m}^3$, $E = 500p\text{kPa}$, $\nu = 0.3$, $\phi_{\max} = 40^\circ$, $\phi_{\text{cr}} = 35^\circ$, $\beta_{\max} = 12^\circ$, $\beta_{\text{cr}} = 0^\circ$, $\gamma_p^p = 0.05$, $\gamma_{\text{cr}}^p = 0.20$, $d_{50} = 0.50\text{mm}$, $a_1 = 0.30$, $a_2 = 0.20$, $a_3 = 1$) are shown in Figure 12 and those for loose sand ($\gamma_d = 14.50\text{kN/m}^3$, $E = 500p\text{kPa}$, $\nu = 0.3$, $\phi_{\max} = \phi_{\text{cr}} = 35^\circ$, $\beta_{\text{cr}} = 0^\circ$, $\gamma_{\text{cr}}^p = 0.05$, $d_{50} = 0.50\text{mm}$, $a_1 = 0.30$, $a_2 = 0.20$, $a_3 = 1$) are shown in Figure 13.

A decrease of the initial sand density causes smaller changes of the T, N and P forces, horizontal stresses, σ_{11}, and wall friction angle, φ_w, during silo flow. The maximum wall friction force decreases with decreasing initial density. Thus, the minimum bottom force decreases with increasing initial density. The maximum horizontal wall force is greater for medium dense sand than for dense sand (as in the experiment [1]). The residual wall forces are similar independently of the initial

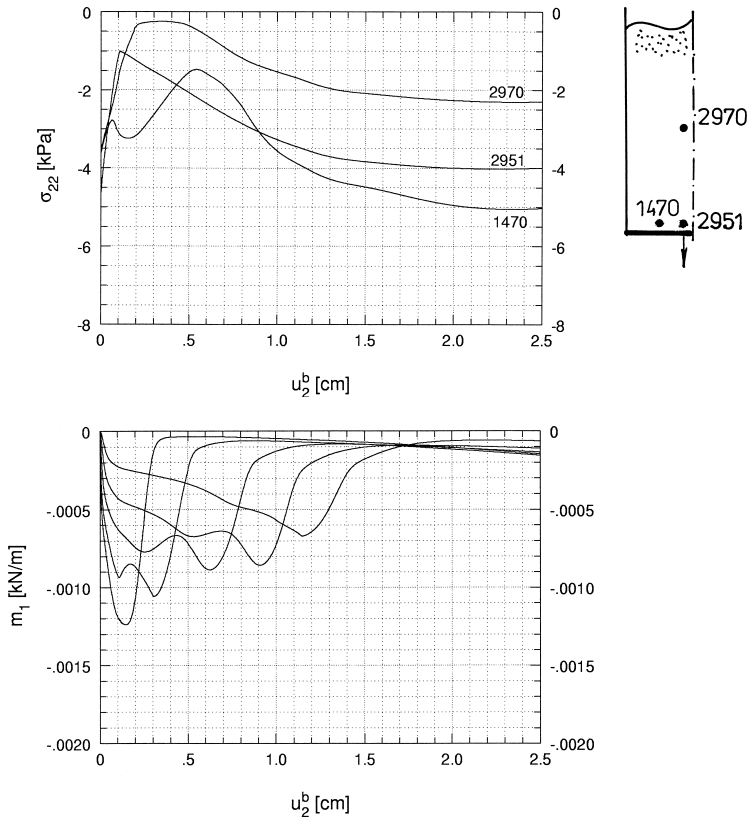

Figure 7. Calculated vertical normal stresses, σ_{22}, and wall couple stresses, m_1, versus bottom displacement, u_2^b, at various points of the silo fill (dense sand, very rough walls)

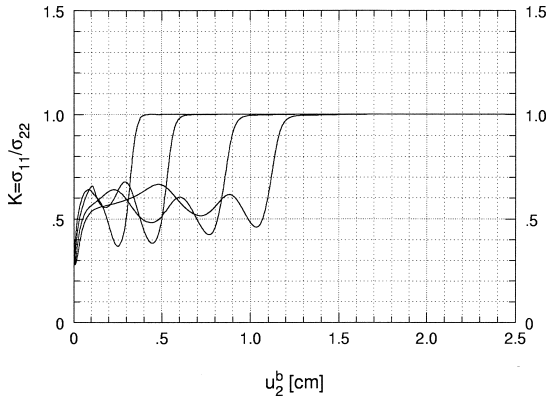

Figure 8. Calculated pressure coefficients, K, versus bottom displacement, u_2^b, at various points along the wall (dense sand, very rough walls)

sand density. The thickness of the wall shear zone increases with decreasing initial solid density. The thickness of the wall shear zone is about 17.5mm and 17.2mm for loose and medium dense sand, respectively. The maximum horizontal wall stresses σ_{11} are about 2.8kPa (medium dense sand) and 1.8kPa (loose sand). The peaks of

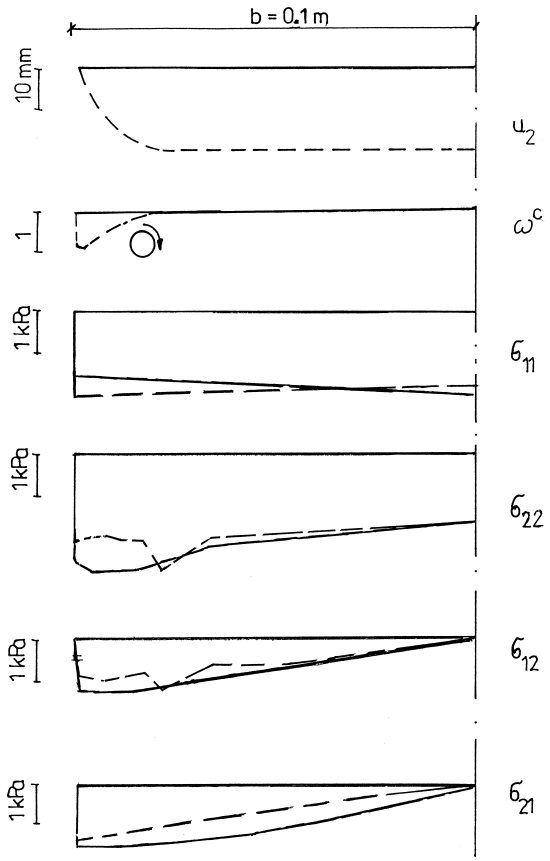

Figure 9. Calculated vertical displacement, u_2, Cosserat rotation, ω^c, and stresses, σ_{ij}, along the silo width in the middle of the silo (dense sand, very rough walls); —— $u_2^b = 1.25\text{mm}$, – – – $u_2^b = 25\text{mm}$

σ_{11} are less displaced in time than for dense sand. The tendency to stress oscillation diminishes with decreasing initial density. The maximum resultant wall friction angles are $\varphi_w = 42^\circ$ (medium dense sand) and $\varphi_w = 38^\circ$ (loose sand). The residual wall friction angle is $\varphi_w = 32^\circ$. The mean volume changes in the residual state are $(u-w)/h = 0.01$ (medium dense sand) and $(u-w)/h = -0.01$ (loose sand). They are twice those of the experiments.

6.2. Influence of wall roughness

The calculations were carried out only with dense sand ($\gamma_d = 16.75\text{kN/m}^3$, $E = 500p\text{kPa}$, $\nu = 0.3$, $\phi_{\max} = 47^\circ$, $\phi_{\text{cr}} = 35^\circ$, $\beta_{\max} = 28.3^\circ$, $\beta_{\text{cr}} = 0^\circ$, $\gamma_p^p = 0.05$, $\gamma_{\text{cr}}^p = 0.20$, $d_{50} = 0.50\text{mm}$, $a_1 = 0.30$, $a_2 = 0.20$, $a_3 = 1.0$). The FE results for smooth walls ($r_w = d_{50}/20$) are demonstrated in Figure 14. The results of forces are in good accordance with the experiment. The changes of P and T are small after bottom displacement. At the same time, the changes of N are greater. The maximum horizontal wall stresses are significantly smaller than for very rough walls. The thickness of the wall shear zone is equal to d_{50}. In comparison with the experiment, the increase of the horizontal wall force N during flow is excessive. Additionally,

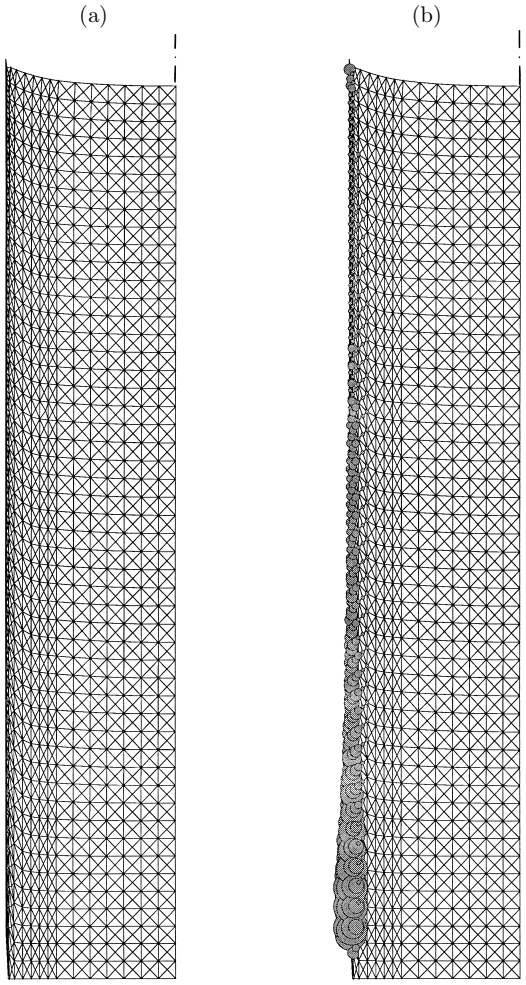

Figure 10. Calculated displacements (a) and Cosserat rotations (b) in a model silo with dense sand and very rough walls in the residual state ($u_2^b = 25$mm)

the maximum wall friction angle, $\varphi_w = 20^\circ$, is 2° too great, and the residual wall friction angle, $\varphi_w = 9.5^\circ$, is 5° too small. However, the FE calculations demonstrate that the increase of N can be reduced by an increase of the difference between a_1 and a_2.

Figures 15 and 16 present results for the model silo with rough walls ($r_w = d_{50}/4$ and $r_w = d_{50}/2$). The increase of wall roughness contributes to greater force and stress changes after bottom displacement. The greater wall roughness, the greater the wall friction force, the wall friction angle, wall stresses and the thickness of the wall shear zone, and the smaller the drop of the bottom force and the increase of wall forces after bottom displacement. The resultant normal force on the wall in the residual state is slightly higher for $r_w = d_{50}/2$ than for very rough walls (as in the experiment). The maximum wall friction angles are $\varphi_w = 45^\circ$ ($r_w = d_{50}/4$) and $\varphi_w = 47^\circ$ ($r_w = d_{50}/2$). They are too high compared with the experiment. The maximum horizontal stresses on the wall are about 2kPa ($r_w = d_{50}/4$) and 3.6kPa

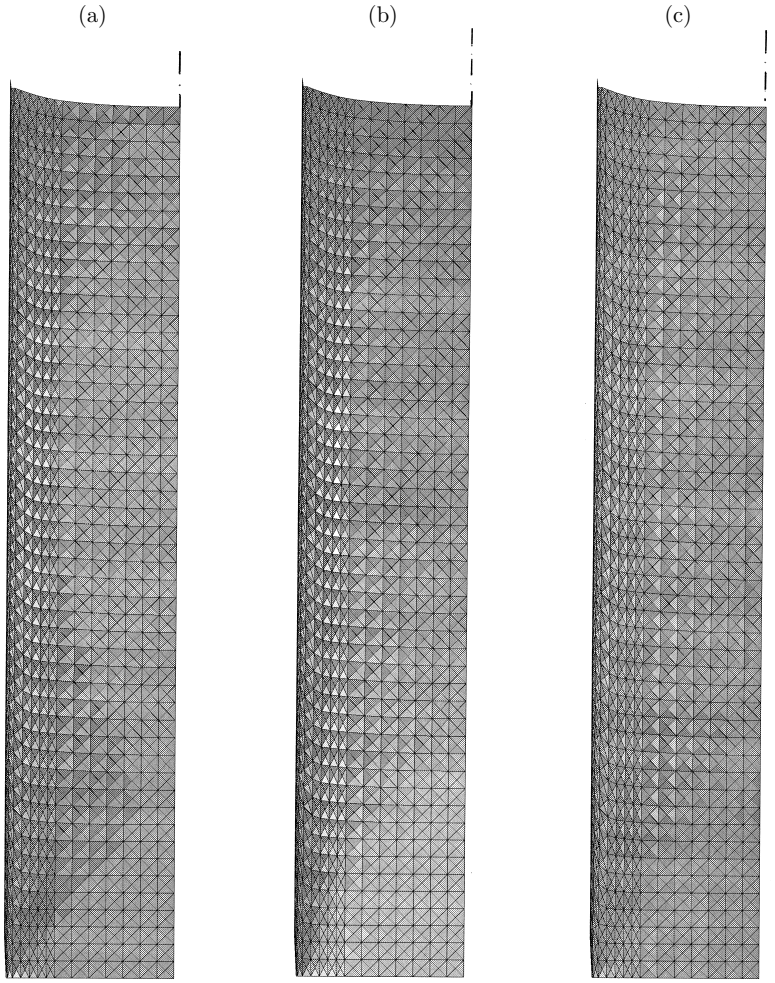

Figure 11. Calculated stresses (a) σ_{11}, (b) σ_{22} and (c) σ_{21} in a silo with dense sand and very rough walls in the residual state ($u_2^b = 25\,\mathrm{mm}$)

($r_w = d_{50}/2$). In the latter case, they are similar to those obtained for very rough walls. The thickness of the wall shear zone is equal to d_{50} ($r_w = d_{50}/4$) or 17mm ($r_w = d_{50}/2$).

In general, the calculated FE results compare well with the experimental values. The essential flow properties of granular materials in silos with different initial fill density and wall roughness observed in the model tests were described realistically. The existing differences between the experimental and the theoretical results may be due to various factors. First, the experiments were performed in a rectangular bin, where the effect of perspex walls occurred. In turn, the FE calculations were carried out for the case of plane strain. Second, symmetry with respect to the centre line was assumed. However, flow of dense sand is always non-symmetric due to the formation of shear zones inside the solid. Third, the constitutive model used is too simple to describe the complex behaviour of granular bodies during flow. Therefore, to achieve better agreement between calculations and experiments,

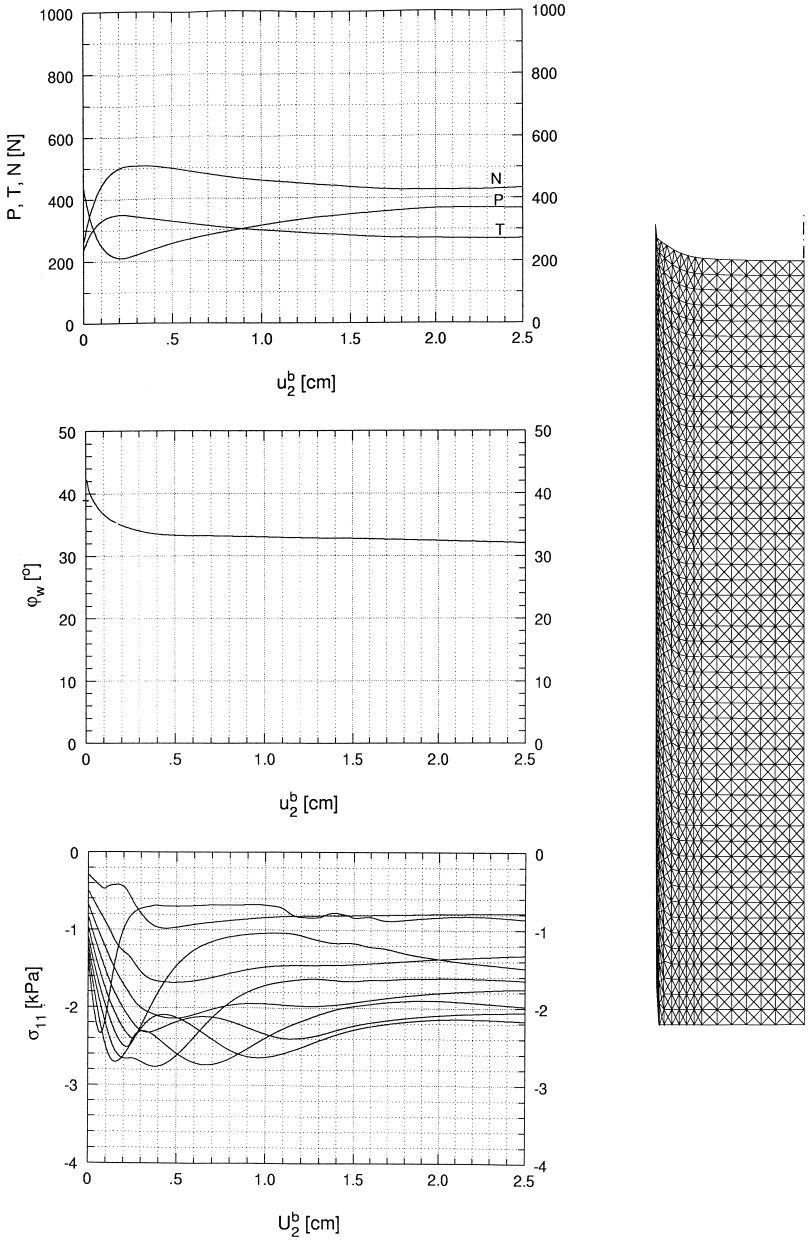

Figure 12. FE results (medium dense sand, very rough walls): evolution of resultant forces P, T, N, wall friction angle, $\varphi_w = \mathrm{arctg}(T/N)$, and horizontal normal stresses, σ_{11}, at various points along the wall versus bottom displacement, u_2^b, and deformed mesh in the residual state ($u_2^b = 25\,\mathrm{mm}$); T – vertical wall friction force, N – horizontal wall force, P – vertical bottom force

a more realistic constitutive model should be used, *e.g.* a polar hypoplastic one ([4, 43, 63]), obtained by the extension of the non-polar hypoplastic model ([66–68]) with polar quantities. It also takes into account such important material properties as: dependence on the stress level, on the material density and on the direction of

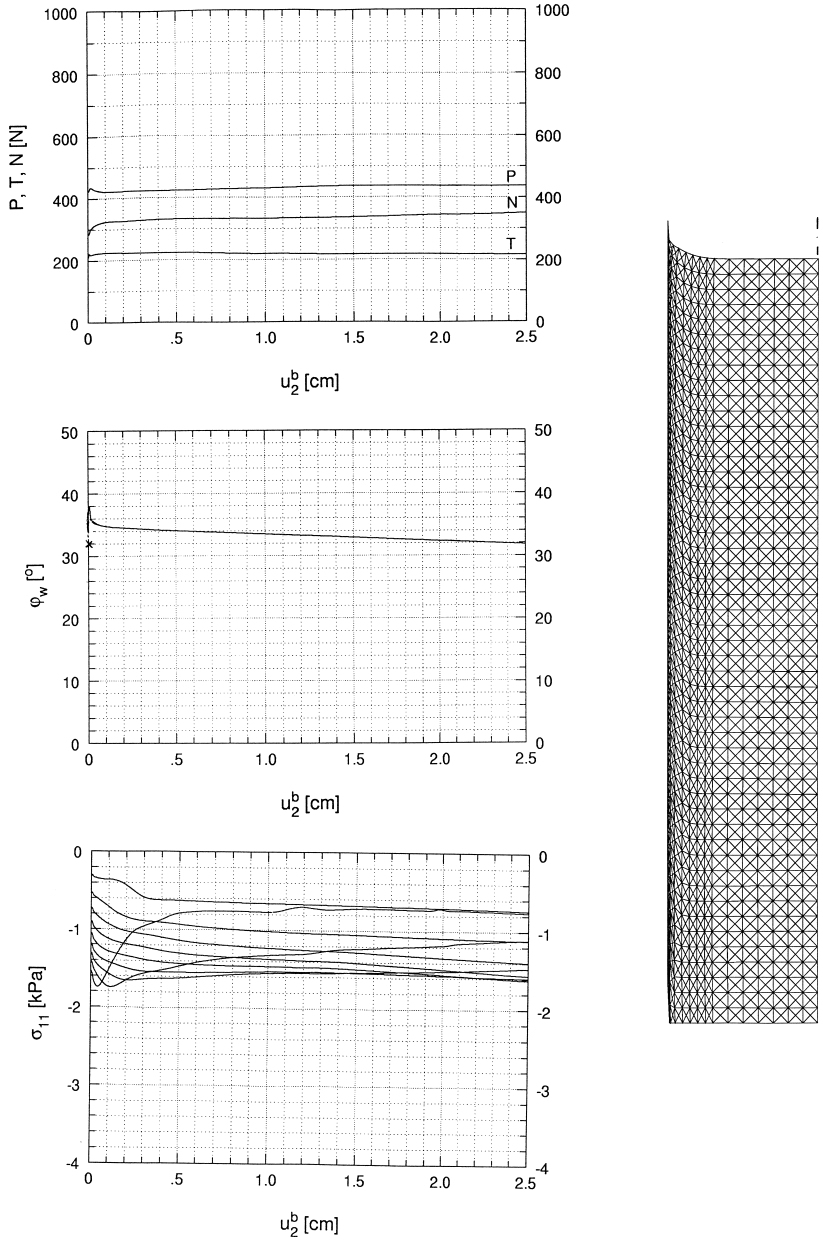

Figure 13. FE results (loose sand, very rough walls): evolution of resultant forces P, T, N, wall friction angle, $\varphi_w = \mathrm{arctg}(T/N)$, and horizontal normal stresses, σ_{11}, at various points along the wall versus bottom displacement, u_2^b, and deformed mesh in the residual state ($u_2^b = 25\mathrm{mm}$) T – vertical wall friction force, N – horizontal wall force, P – vertical bottom force

deformation: the transition between dilatancy and contractancy during shearing with a constant pressure; and the transition between the pressure increase and pressure release during shearing with a constant volume. Advantages of the model are its simplicity and the simple procedure for determination of material constants with standard laboratory experiments. At the same time, the obtained results for smooth

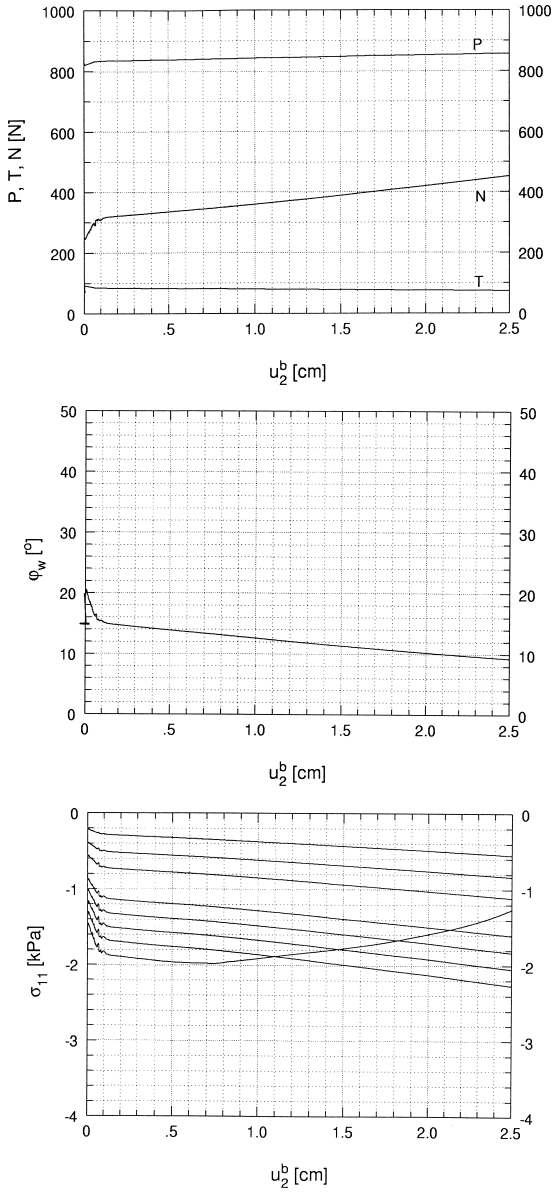

Figure 14. FE results (dense sand, rough walls, $r_w = d_{50}/20$): evolution of resultant forces P, T and N, wall friction angle, $\varphi_w = \mathrm{arctg}(T/N)$, and horizontal normal stresses, σ_{11}, at various points along the wall versus bottom displacement, u_2^b; T – vertical wall friction force, N – horizontal wall force, P – vertical bottom force

and rough walls are strongly dependent upon the polar constants. Therefore, to obtain better agreement with experimental results, further FE studies on polar boundary conditions are necessary.

6.3. Influence of the modulus of elasticity

Figure 17 demonstrates the results for dense sand with a constant modulus of elasticity in a silo with very rough walls ($\gamma_d = 16.75\mathrm{kN/m^3}$, $\nu = 0.3$, $\phi_{\max} = 47^\circ$,

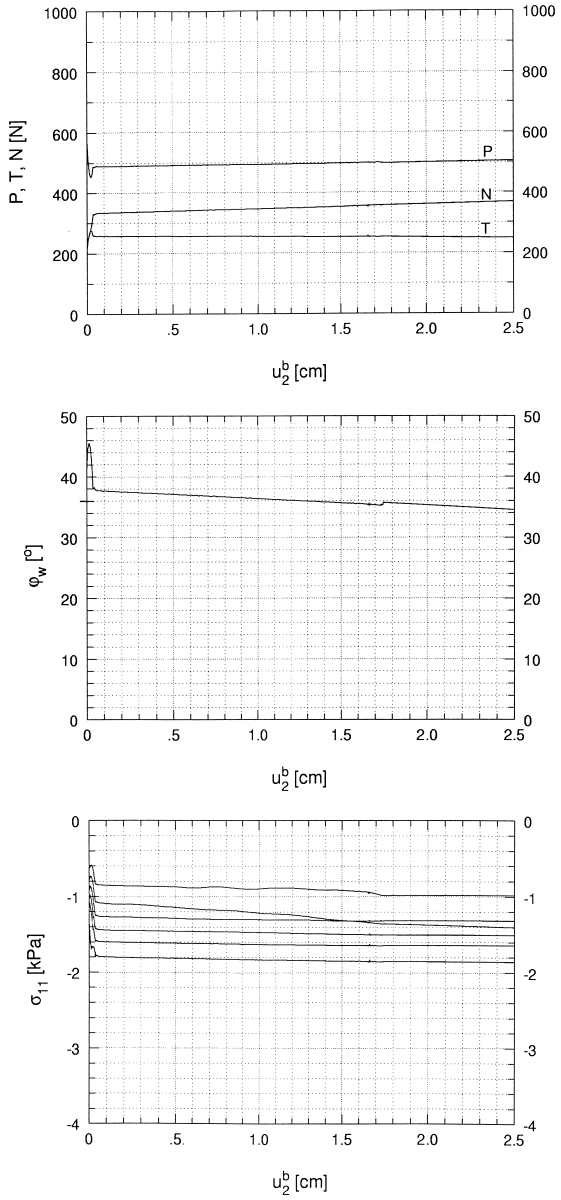

Figure 15. FE results (dense sand, rough walls, $r_w = d_{50}/4$): evolution of resultant forces P, T and N, wall friction angle, $\varphi_w = \mathrm{arctg}(T/N)$, and horizontal normal stresses, σ_{11}, at various points along the wall versus bottom displacement, u_2^b; T – vertical wall friction force, N – horizontal wall force, P – vertical bottom force

$\phi_{\mathrm{cr}} = 35^{\circ},\ \beta_{\max} = 28.3^{\circ},\ \beta_{\mathrm{cr}} = 0^{\circ},\ \gamma_p^p = 0.05,\ \gamma_{\mathrm{cr}}^p = 0.20,\ d_{50} = 0.50\mathrm{mm},\ a_1 = 0.30,$ $a_2 = 0.20,\ a_3 = 1.0$). By assuming a constant modulus E, a greater oscillation of the resultant forces and wall stresses is obtained. An increase of E causes an increase of the maximum wall forces and residual bottom forces, and a drop in the minimum bottom force and residual wall forces. The horizontal wall stresses and the thickness of the wall shear zone are slightly smaller (by 10%) than those for a variable elastic

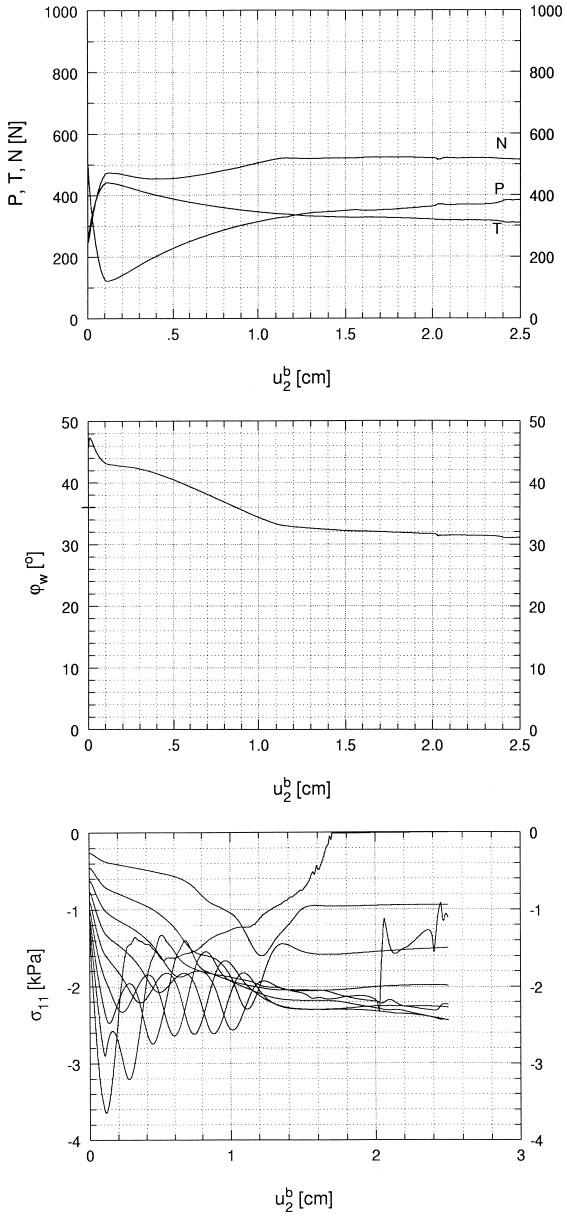

Figure 16. FE results (dense sand, rough walls, $r_w = d_{50}/2$): evolution of resultant forces P, T and N, wall friction angle, $\varphi_w = \mathrm{arctg}(T/N)$, and horizontal normal stresses, σ_{11}, at various points along the wall versus bottom displacement, u_2^b; T – vertical wall friction force, N – horizontal wall force, P – vertical bottom force

modulus E estimated with Equation (20). The maximum of σ_{11} on the wall is not influenced by E.

6.4. Influence of the initial stress state

The calculated resultant forces P, T and N for the initial stress state K_0 ($\sigma_{22} = \gamma_d x_2,\ \sigma_{11} = K_0\sigma_{22},\ \sigma_{12} = \sigma_{21} = 0,\ m_1 = m_2 = 0,\ K_0 = 0.45$) with dense sand

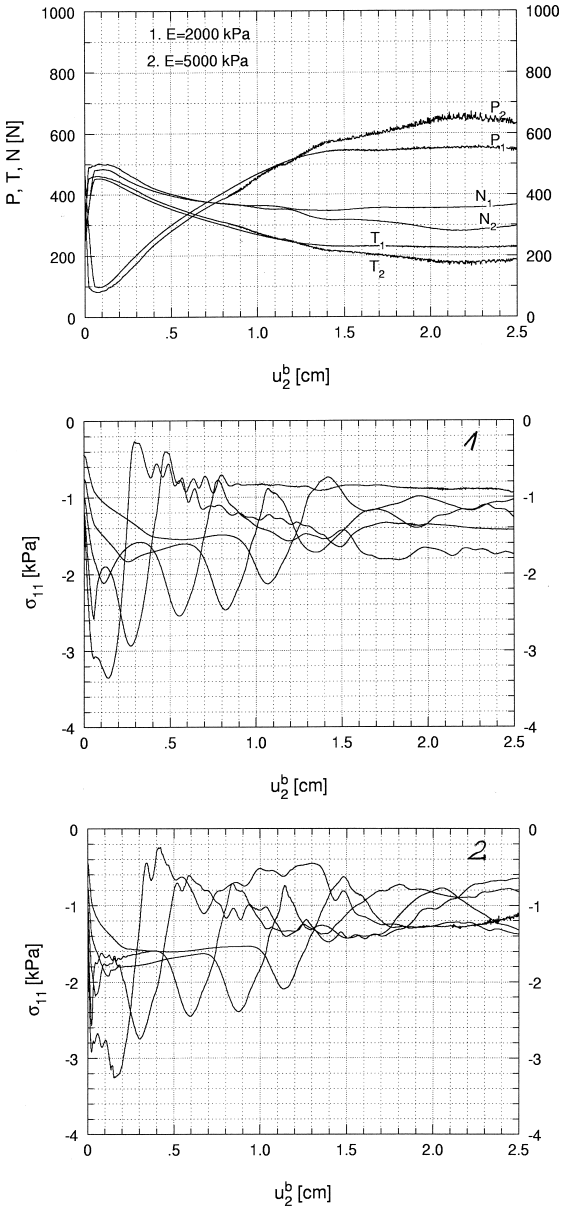

Figure 17. FE results (dense sand and very rough walls, $d_{50} = 0.5$mm): evolution of resultant forces P, T, N and horizontal normal stresses, σ_{11}, at various points along the wall versus bottom displacement, u_2^b; T – vertical wall friction force, N – horizontal wall force, P – vertical bottom force; 1 – $E = 2\,000$kPa, 2 – $E = 5\,000$kPa

and very rough walls are presented in Figure 18. The assumption of an initial stress state (assuming no shear stresses) has little effect on the calculated forces at the beginning of the flow. The differences are more noticeable in the residual state. In this case, the T and N forces are slightly stronger, and the P force is slightly weaker. The effect of the initial stress state on horizontal wall stresses is insignificant.

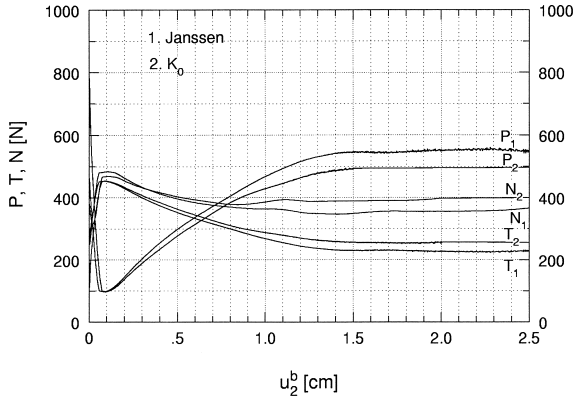

Figure 18. FE results (dense sand and very rough walls, $E=2\,000$kPa, $d_{50}=0.5$mm): evolution of resultant forces P, T, N versus bottom displacement, u_2^b, for the initial stress state: 1 – by Janssen and 2 – the K_0-initial stress state; T – vertical wall friction force, N – horizontal wall force, P – vertical bottom force

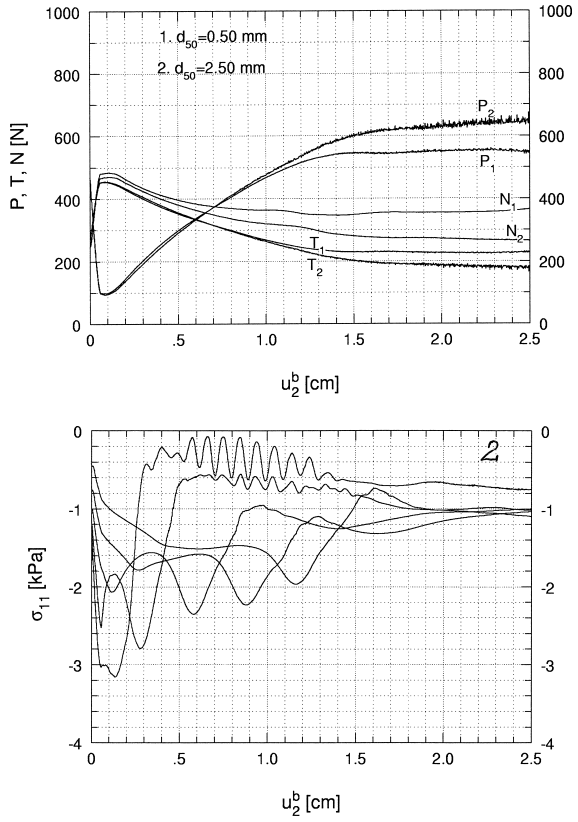

Figure 19. FE results (dense sand and very rough walls, $E=2\,000$kPa): evolution of resultant forces P, T, N and horizontal normal stresses, σ_{11}, at various points along the wall versus bottom displacement, u_2^b; T – vertical wall friction force, N – horizontal wall force, P – vertical bottom force; 1 – $d_{50}=0.5$mm, 2 – $d_{50}=2.5$mm

6.5. Influence of the mean grain diameter

Figure 19 shows dense-sand-and-very-rough-walls results for a greater mean grain diameter ($d_{50} = 2.5$mm). An increase of d_{50} increases the residual bottom force P and decreases the residual wall forces T and N. The residual normal force N is smaller by 20% (dense sand) or by 5% (medium dense sand) for $d_{50} = 2.5$mm. The maximum wall stresses are almost the same. The thickness of the wall shear zone, 18mm ($d_{50} = 2.5$mm), is slightly greater than for $d_{50} = 0.50$mm. The wall friction angles are slightly higher for larger grains. The maximum and residual resultant wall friction angles (dense sand, $d_{50} = 2.5$mm) are $\varphi_w = 49^\circ$ and $\varphi_w = 34^\circ$, respectively. In the case of medium dense sand with $d_{50} = 2.5$mm and dense sand with $d_{50} = 0.1$mm, the thickness of the wall shear zone is about 20mm and 8mm, respectively. The influence of d_{50} on maximum wall stresses is minimal. The effect of d_{50} on the obtained results decreases with decreasing initial sand density. It should be noted that an increase of the internal friction angle and the dilatancy angle with increasing mean grain diameter was neglected in the calculations [4]. If considered, this dependency would increase the wall forces for larger grains. The influence of d_{50} on γ_d was likewise not considered. In general, the larger the grains, the smaller the initial density.

6.6. Influence of the polar constants

The calculations were carried out for dense sand and very rough walls using $a_1 = 0.375$, $a_2 = 0.125$, $a_3 = 1$. These constants were proposed by Mühlhaus [49] in the so-called kinematic polar model. In this case, the polar shear modulus and the non-symmetry of the stress tensor are smaller than for $a_1 = 0.3$ and $a_2 = 0.2$ [4, 51]. According to the kinematic model, the maximum and residual wall forces are weaker (Figure 20). The thickness of the wall shear zone on the basis of the Cosserat rotation, 15mm, is also smaller.

6.7. Influence of wall stiffness

In order to approximately model a flexible wall, horizontal elastic springs with constant stiffness were prescribed to nodes along the entire vertical wall. In one case we chose the spring stiffness of $k = 200$kN/m, and in another case – $k = 50$kN/m. The results (Figures 21 and 22) show that the more flexible the wall, the greater changes of forces can be observed during flow. For the greater spring stiffness of $k = 200$kN/m, the residual wall forces and maximum horizontal wall stresses are smaller compared to a rigid wall. For the lower spring stiffness of $k = 50$kN/m, the evolution of wall forces and residual wall stresses is entirely different than for a rigid wall. Both wall forces and residual wall stresses are significantly higher due to a high wall curvature. In this case, a small part of the wall (below 3.5cm) is displaced towards the symmetry axis. However, the part remaining above is curved to the outside. The maximum outward wall displacement at the silo height of about 10cm is about 0.40–0.45mm. The outward displacement is subsequently reduced toward the wall's top. The thickness of the wall shear zone along flexible walls is almost the same as for rigid walls.

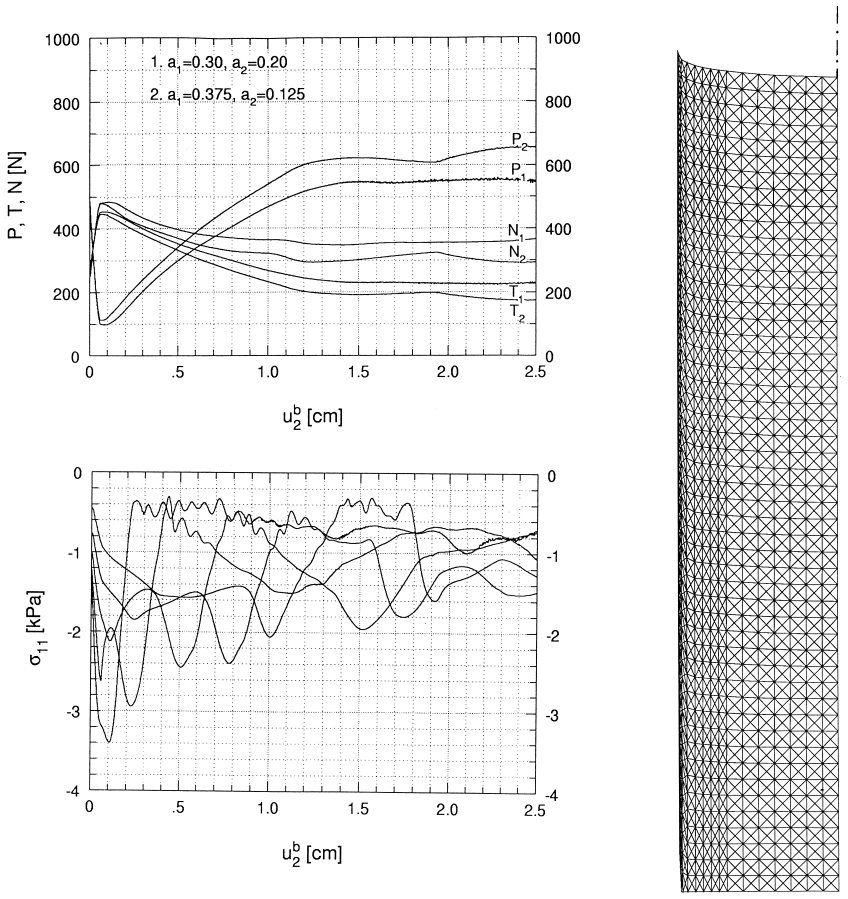

Figure 20. FE results (dense sand, very rough walls, $E = 2\,000$kPa, $d_{50} = 0.5$mm): evolution of resultant forces P, T, N and horizontal normal stresses, σ_{11}, at various points along the wall versus bottom displacement, u_2^b, and deformed mesh in the residual state ($u_2^b = 25$mm); T – vertical wall friction force, N – horizontal wall force, P – vertical bottom force; 1 – $a_1 = 0.30$, $a_2 = 0.20$, 2 – $a_1 = 0.375$, $a_2 = 0.125$

6.8. Influence of wall imperfection

An imperfection was assumed in the form an initial horizontal displacement of three wall nodes to the inside and to the outside, 40mm in length, at the height of $h = 100$mm above the silo's bottom. The horizontal wall displacement was taken as 2mm. The FE results (Figure 23) show that this small imperfection directed inwards increases the maximum horizontal wall stresses (by about 25%) and decreases them (by about 5%) when directed outwards (Figure 17).

6.9. Influence of the pressure level

The calculations were carried out with a silo 10 times larger ($h = 5.0$m, $b = 2.0$m) [62]. During calculations, a decrease of the internal friction angle and the dilatancy angle and an increase of shear deformation at peak with increasing pressure level was assumed [69]. The analysis was performed with $\gamma_d = 16.30\text{kN/m}^3$, $\phi_{\max} = 43^\circ$, $\beta_{\max} = 19^\circ$, $E = 500p$kPa, $\gamma_p^p = 0.10$ and $d_{50} = 0.5$mm. The normalised

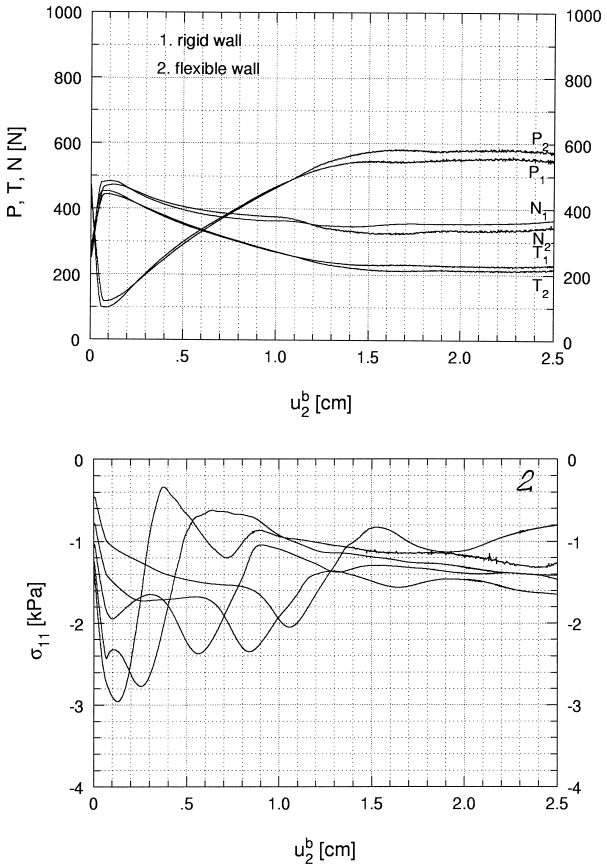

Figure 21. FE results (dense sand, very rough walls, $E = 2\,000$kPa, $d_{50} = 0.5$mm): evolution of resultant forces P, T, N and horizontal normal stresses, σ_{11}, at various points along the wall versus bottom displacement, u_2^b; T – vertical wall friction force, N – horizontal wall force, P – vertical bottom force; 1 – rigid wall, 2 – flexible wall ($k = 200$kN/m)

resultant wall forces (Figure 24) show that the minimum bottom and the maximum wall friction force's are weaker, and the maximum horizontal wall force is stronger than for the smaller silo. At the residual state, the wall forces are stronger and the bottom force is weaker. The maximum normalised horizontal wall stresses are 5% smaller compared to the model silo. The thickness of the shear zone is about 17cm. The calculations indicate that the results from model silos cannot be directly transferred to large silos due to effects of scale.

6.10. Influence of small deformations and curvatures

An analysis was performed for small deformations and curvatures (Figure 25). In this case, the stresses and couple stresses were calculated without taking into consideration the Jaumann terms, and the changes of element configuration and volume were neglected. The effect of large deformations and curvatures begins to be noticeable at the bottom displacement of $u_2^b = 7$mm. The residual wall forces T and N are stronger and the residual bottom force P is weaker for large deformations and curvatures.

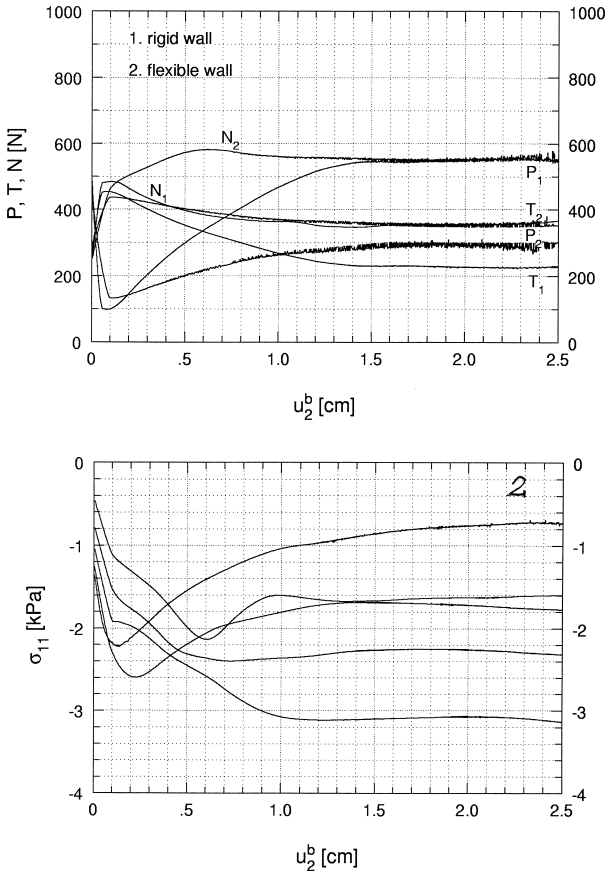

Figure 22. FE results (dense sand, very rough walls, $E = 2\,000\,\mathrm{kPa}$, $d_{50} = 0.5\,\mathrm{mm}$): evolution of resultant forces P, T, N and horizontal normal stresses, σ_{11}, at various points along the wall versus bottom displacement, u_2^b; T – vertical wall friction force, N – horizontal wall force, P – vertical bottom force; 1 – rigid wall, 2 – flexible wall ($k = 50\,\mathrm{kN/m}$)

7. Conclusions

The FE calculations show that quasi-static mass flow of granular bodies in silos can be described with a polar elasto-plastic constitutive model. The model captures the salient properties of granular materials during confined granular flow. The obtained numerical results are in satisfactory agreement with the experimental ones, in spite of the simplicity of the model used. The following observations can be made on the basis of the FE calculations:

The calculated forces and stresses in granular materials during silo emptying are very sensitive to the initial density of the silo fill, wall roughness, wall stiffness and imperfections, the modulus of elasticity, the mean grain diameter of the bulk solid, and the micro-polar coefficients.

The maximum resultant wall friction force increases with increasing initial solid density and wall roughness. Thus, the minimum resultant bottom force decreases with increasing initial density and wall roughness. The changes of forces during granular flow increase with increasing initial density and wall roughness.

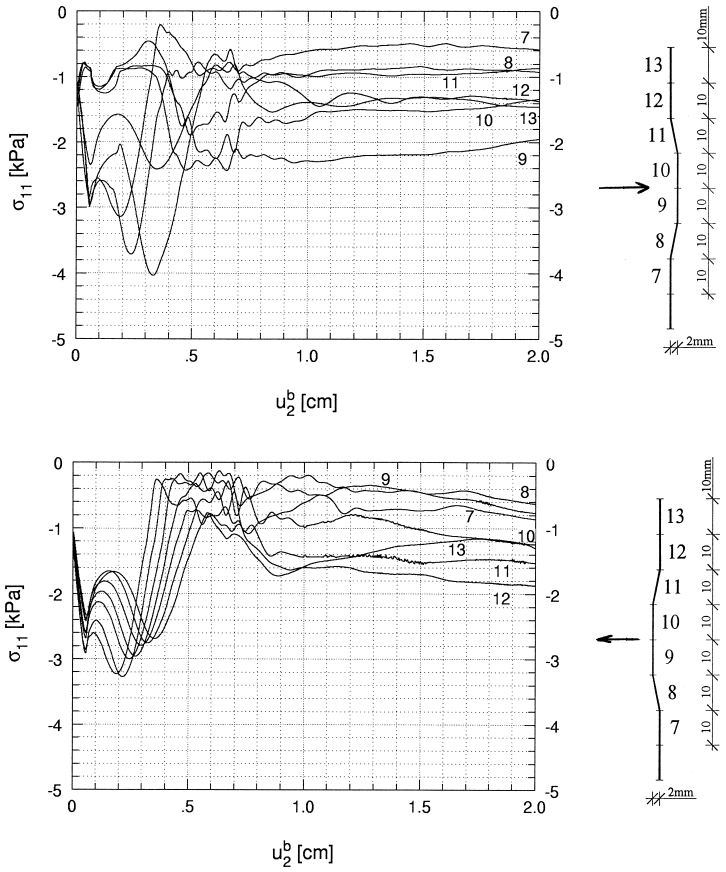

Figure 23. FE results (dense sand, very rough walls with an imperfection, $E = 2\,000$kPa, $d_{50} = 0.5$mm): horizontal normal stresses, σ_{11}, at different points along the wall versus bottom displacement, u_2^b: top – imperfection directed inwards, bottom – imperfection directed outwards

The horizontal wall stresses have a tendency to oscillate, which increases with increasing fill density. The maximum horizontal wall stresses increase with increasing initial solid density. For dense sand, they increase with increasing wall roughness. They are sensitive to wall imperfections and wall flexibility. Wall imperfections directed inwards significantly increase wall stresses, while wall imperfections directed outwards decrease them slightly. In the case of flexible walls, the maximum horizontal wall stresses are smaller and the residual ones are greater.

Wall stresses can be greater than these calculated with silo codes, in particular for dense sand and very rough walls. In general, the stresses are non-uniformly distributed in bulk solids. Their non-uniformity increases with increasing initial density and wall roughness.

Due to the effect of the pressure level and grain rotations in the wall shear zone, the results from model tests cannot be transferred to large silos.

The polar approach is very effective as a regularisation method when shear localisation is dominant. The calculated thickness of wall shear zones increases with decreasing initial fill density and increasing wall roughness and mean grain diameter.

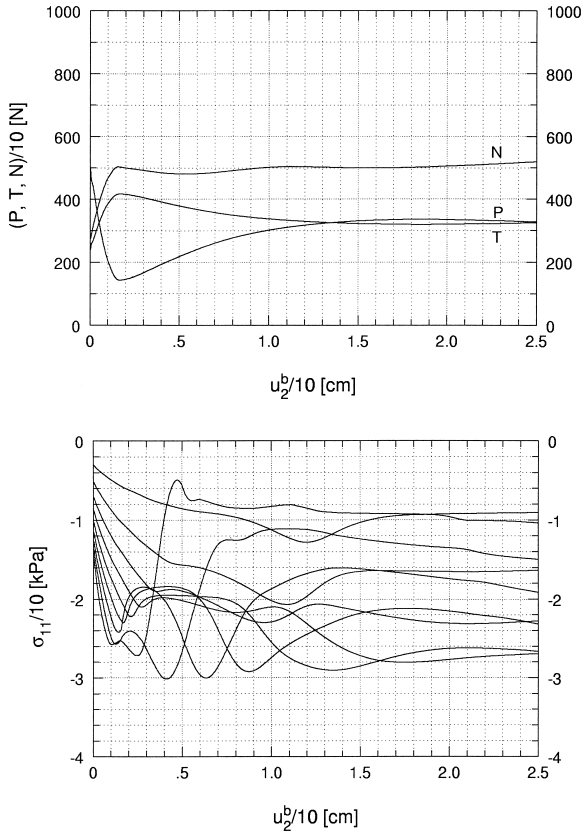

Figure 24. FE results in a large silo (dense sand, very rough walls, $h = 5.0$m, $b = 0.2$m, $E = 500p$, $d_{50} = 0.5$mm): normalised resultant forces P, T, N and horizontal normal stresses, σ_{11}, at various points along the wall versus bottom displacement, u_2^b; T – vertical wall friction force, N – horizontal wall force, P – vertical bottom force

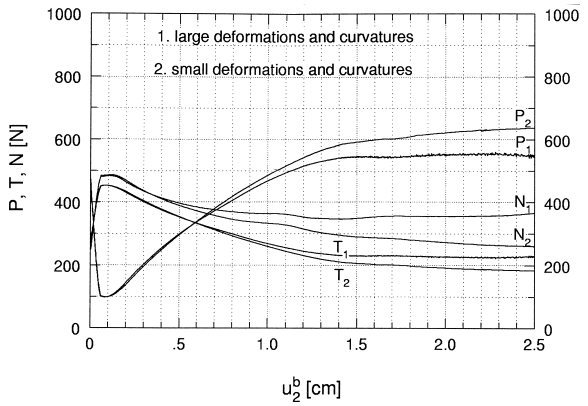

Figure 25. FE results (dense sand, very rough walls, $E = 2\,000$kPa, $d_{50} = 0.5$mm): evolution of resultant forces P, T and N versus bottom displacement, u_2^b; 1 – large deformations and curvatures, 2 – small deformations and curvatures

Cosserat rotations and couple stresses are only noticeable in shear zones. The Cosserat rotation is a suitable indicator of shear zones. A polar granular body is stronger and stiffer than a non-polar one.

The numerical analysis of quasi-static flow of granular materials in silos with a polar hypoplastic constitutive model will be carried out [70]. The results will be re-checked with model tests. Numerical simulations will be carried out for the entire silo. The initial void ratio of the solid will be stochastically distributed in the silo using a random generator.

References

[1] Tejchman K 1989 *Publication Series of the Institute for Rock and Soil Mechanics*, Karlsruhe University, Germany **117** pp. 1–236

[2] Tejchman J and Gudehus G 1993 *Powder Technology* **76** (2) 201

[3] Tejchman J 1993 *Archives of Civil Engineering*, Polish Academy of Sciences, Warsaw **1** pp. 7–28

[4] Tejchman J 1997 *Publication Series of the Institute for Rock and Soil Mechanics*, Karlsruhe University, Germany **140** pp. 1–353

[5] Więckowski Z 1998 *Computational Mechanics* (Idelsohn S, Onate E and Dvorkin E, Eds), CIMNE, Barcelona, Spain, pp. 1–20

[6] Häußler U and Eibl J 1984 *J. Engng. Mech.* **110** 975

[7] Eibl J and Rombach G 1988 *Int. Conf. Silos-Forschung und Praxis*, Karlsruhe University, Germany, SFB **219** pp. 1–15

[8] Vedaie B and Bishara A G 1988 *Int. Conf. Silos-Forschung und Praxis*, Karlsruhe University, Germany, SFB **219** pp. 25–55

[9] Gudehus G and Tejchman J 1991 *Advances in Continuum Mechanics* (Brüller O, Mannel V and Najar J, Eds), Springer Verlag, Berlin, Heidelberg, pp. 178–193

[10] Tano E, Godoy L A and Diez M A 1994 *Comput. Meth. Adv. Geomech.* **2** 1281

[11] Ragneau E and Aribert J M 1995 *Proc. 3rd Europ. Symp. on Storage and Flow of Particulate Solids, PARTEC95*, Nürnberg, Germany, pp. 205–219

[12] Ruckenbrod C and Eibl J 1995 *Proc. 3rd Europ. Symp. Storage and Flow of Particulate Solids, PARTEC 95*, Nürnberg, Germany, pp. 193–202

[13] Tejchman J 1995 *Proc. 3rd Europ. Symp. Storage and Flow of Particulate Solids, PARTEC 95*, Nürnberg, Germany, pp. 151–163

[14] Savage S B 1992 *Physics of Granular Media* (Bideau D and Dodds J, Eds), Nova Science Publishers Inc., pp. 343–362

[15] Sakaguchi H and Ozaki E 1993 *Powders and Grains* (Thornton C, Ed.), Balkema, Rotterdam, pp. 351–357

[16] Thornton C and Sun G 1993 *Powders and Grains* (Thornton C, Ed.), Balkema, Rotterdam, pp. 129–134

[17] Kafui K D and Thornton C 1997 *Powders and Grains* (Behringer R P and Jenkins J T, Eds), Balkema, Rotterdam, pp. 511–514

[18] Langston P A, Heyes D M and Tüzün U 1995 *Proc. 3rd Europ. Symp. Storage and Flow of Particulate Solids, PARTEC 95*, Nürnberg, Germany, pp. 357–367

[19] Gutfraind R and Pouliquen O 1996 *Mechanics of Materials* **24** 273

[20] Luding S, Duran J, Clement E and Rejchenbach J 1996 *Proc. 5th World Congress of Chemical Engineering*, San Diego **5** pp. 325–330

[21] Ristow G H 1997 *Powders and Grains* (Behringer R P and Jenkins J T, Eds), Balkema, Rotterdam, pp. 527–530

[22] Haff P K 1983 *J. Fluid Mech.* **134** 401

[23] Jenkins J T and Richman M W 1985 *Phys. Fluids* **28** 3485

[24] Lun C K K and Savage S B 1987 *J. Appl. Mech.* **54** 47

[25] Jenkins J T 1992 *J. Appl. Mech.* **59** 120

[26] Fütterer G 1991 *Untersuchungen zum schnellen Fließen von trockenen, kohäsionslosen Schüttgütern in konvergenten Schächten*, Dissertation, Karlsruhe University, Germany, pp. 1–140
[27] Baxter G W and Behringer R P 1990 *Two Phase Flows and Waves*, Springer Verlag, New York, pp. 1–29
[28] Martinez J, Masson S and Deserable D 1995 *Proc. 3rd Europ. Symp. Storage and Flow of Particulate Solids, PARTEC 95*, Nürnberg, Germany, pp. 367–379
[29] Tejchman J 1992 *Archives of Civil Engineering*, Polish Academy of Sciences, Warsaw **4** pp. 375–394
[30] Tejchman J 1992 *Archives of Civil Engineering*, Polish Academy of Sciences, Warsaw **4** pp. 395–414
[31] Uesugi M 1987 *Friction between Dry Sand and Construction*, Dissertation, Tokyo Institute of Technology
[32] Uesugi M, Kishida H and Tsubakihara Y 1988 *Soils and Foundations* **28** (1) 107
[33] Janssen H A 1985 *VDI Zeitschrift* **39** 1045
[34] Günther W 1958 *Zur Statik und Kinematik des Cosserat-Kontinuums*, Abh. Braunschweigische Wiss. **10** pp. 195–213
[35] Schäfer H 1962 *Miszellaneen der Angewandten Mechanik, Festschrift Tolmien*, W., Berlin, Akademie-Verlag, pp. 277–292
[36] Mühlhaus H B 1987 *Veröffentlichungen des Institutes für Boden- und Felsmechanik* (106), Karlsruhe University, Germany
[37] Mühlhaus H B 1989 *Int. J. Num. Anal. Meth. Geomech.* **13** 545
[38] Sluys L J 1992 *Wave Propagation, Localisation and Dispersion in Softening*, Dissertation, Delft University, pp. 1–163
[39] Benallal A, Billardon R and Geymonat G 1991 *Proc. 3rd Int. Conf. Constitutive Laws for Engineering Materials: Theory and Applications*, Tucson, Arizona, pp. 387–390
[40] de Borst R, Mühlhaus H B, Pamin J and Sluys L Y 1992 *Proc. 3rd Int. Conf. Comp. Plasticity* (Owen D R J, Onate E and Hinton E, Eds), Pineridge Press, Swansea, pp. 483–508
[41] Oda M, Konishi and Nemat-Nasser S 1982 *Mechanics of Materials* **1** 269
[42] Oda M 1993 *Powders and Grains* (Thornton C, Ed.), Rotterdam, Balkema, pp. 161–167
[43] Tejchman J, Herle I and Wehr J 1999 *Int. J. Num. Anal. Meth. Geomech.* **23** 2045
[44] Bogdanova-Bontscheva N and Lippmann H 1975 *Acta Mech.* **21** 93
[45] Becker M and Lippmann H 1977 *Archives of Mechanics* **29** 829
[46] Kanatani K 1979 *Int. J. Eng. Sci.* **17** 419
[47] Mühlhaus H B and Vardoulakis I 1987 *Geotechnique* **37** 271
[48] Mühlhaus H B 1989 *Ing. Arch.* **59** 124
[49] Mühlhaus H B 1990 *Comprehensive Rock Engineering* (Hudson J A and Fairhurst Ch, Eds), Pergamon Press **2** pp. 209–231
[50] Mróz Z 1963 *J. de Mechanique* **1** 21
[51] Tejchman J and Wu W 1993 *Acta Mech.* **99** 61
[52] Vardoulakis I 1980 *Int. J. Num. Anal. Meth. Geomech.* **4** 103
[53] Tejchman J 1994 *Localisation and Bifurcation Theory for Soils and Rocks* (Chambon R, Desrues J and Vardoulakis I, Eds), Balkema, Rotterdam, pp. 257–275
[54] de Borst R 1991 *Engng. Comput.* **8** 317
[55] Papanastasiou P and Vardoulakis I 1992 *Int. J. Num. Anal. Meth. Geomech.* **16** 389
[56] Tejchman J and Wu W 1995 *Int. J. Num. Anal. Meth. Geomech.* **19** (8) 513
[57] Tejchman J and Wu W 1997 *Int. Engng. Mech. J. ASCE* **123** (2) 123
[58] Unterreiner P, Vardoulakis I, Boulon M and Sulem J 1994 *Localisation and Bifurcation Theory for Soils and Rocks* (Chambon R, Desrues J and Vardoulakis I, Eds), Balkema, Rotterdam, pp. 141–155
[59] Steinmann P 1995 *Int. J. Num. Meth. Engng.* **38** 583
[60] Murakami A and Yoshida N 1997 *Deformation and Progressive Failure in Geomechanics* (Asaoka A, Adachi T and Oka F, Eds), Pergamon, pp. 871–876

[61] Groen A E 1997 *Three-dimensional Elasto-plastic Analysis of Soils*, Dissertation, Delft University, pp. 1–113
[62] Tejchman J 2001 *Powder Handling and Processing* **13** (2) 165
[63] Tejchman J 1998 *Powder Technology* **96** (3) 227
[64] Bathe K J 1982 *Finite Element Procedures in Engineering Analysis*, Prentice-Hall, Inc., Englewood Cliffs, New Jersey
[65] Ortiz M and Simo I C 1986 *Int. J. Num. Meth. Engng.* **23** 353
[66] Gudehus G 1996 *Soils and Foundations* **36** (1) 1
[67] Bauer E 1996 *Soils and Foundations* **36** (1) 13
[68] Herle I and Gudehus G 1999 *Mechanics of Cohesive-Frictional Materials* **4** (5) 461
[69] Wu W 1992 *Veröffentlichungen des Institutes für Boden- und Felsmechanik*, Karlsruhe University, Germany **129** pp. 1–154
[70] Tejchman J 2002 *Kona* **20** 125